

**Proton-Mediated Energy Storage in Intermediate-Temperature Solid-Oxide Metal-Air Battery**

Journal:	<i>Journal of Materials Chemistry A</i>
Manuscript ID	TA-COM-08-2018-008180.R1
Article Type:	Communication
Date Submitted by the Author:	03-Oct-2018
Complete List of Authors:	Xu, Nansheng; University of South Carolina, Mechanical Engineering Zhang, Cuijuan; Tianjin University, School of Chemical Engineering and Technology Huang, Kevin; University of South Carolina, Mechanical Engineering



Journal Name

COMMUNICATION

Proton-Mediated Energy Storage in Intermediate-Temperature Solid-Oxide Metal-Air Battery

Received 00th January 20xx,
Accepted 00th January 20xx

Nansheng Xu ^a, Cuijuan Zhang ^b and Kevin Huang ^{a†}

DOI: 10.1039/x0xx00000x

www.rsc.org/

Proton-containing ceramics have been investigated for the first time as the supporting phase for the energy storage medium in intermediate-temperature (IT) solid-oxide metal-air redox battery. The strong interaction between H₂O and oxygen vacancies creates ample protons on the surface of the proton-containing perovskites significantly enhanced the reversibility and cycle performance.

Solid oxide metal-air redox battery (SOMARB) represents a newly emerged class of all solid-state batteries¹⁻¹². Operated on reversible high-temperature oxide-ion chemistry, SOMARB discharges electricity by oxidizing metal into metal-oxide and stores electricity by reducing metal-oxide into metal. During the conversion, the reversible solid oxide fuel cell (RSOFC) is utilized as an electrical discharger/charger via solid oxide fuel cell (SOFC) and solid oxide electrolysis cell (SOEC) modes, respectively, while a metal/oxide chemical bed located in the anode chamber serves as the energy storage medium (ESM). To facilitate the oxygen transfer and avoid direct physical contact between RSOFC-anode and ESM, an oxygen shuttle gas of H₂-H₂O mixture is present in the gap between RSOFC and ESM to mediate the oxygen transfer. At a given temperature, the ratio of partial pressures of H₂ and H₂O is fixed by the thermodynamic equilibrium with Me/MeO_x. In other words, the Nernst potential of SOMARB is an invariant during charge/discharge process. The energy capacity is exclusively determined by the mass of Fe in the ESM with the status of charge being represented by the mass ratio between Me and MeO_x, while the power is solely dependent of RSOFC's electrode surface area.

A key component to the performance of SOMARB is ESM. A functional ESM consists of an active metal and active-metal-coarsening-mitigating oxide phase. From our early studies, it has been shown that Fe is the best ESM material technically as well as economically among all the transition metal-based

systems, and ZrO₂ is the best Fe-sintering-inhibiting oxide component in terms of chemical inertness. As the operating temperature of SOMARB is being pushed toward intermediate range (500-600 °C) to reduce cost and improve reliability, the sluggish kinetics of FeO_x reduction by H₂ has become a major developmental challenge^{6, 13}. To promote the intermediate-temperature FeO_x reduction kinetics, use of nanostructured Fe particles has been proven effective; however, Fe nanoparticles suffer rapid coarsening, resulting in performance degradation. On the other hand, Pd has also been demonstrated an active catalyst for enhancing FeO_x-reduction kinetics because of its unique H-permeation ability. However, the expensive Pd could potentially limit its practical applications.

In the present work, we investigate the effect of proton-containing ceramics as the Fe-supporting oxide (SO) on the performance of SOMARB. There are in general two groups of inorganic materials for proton conductors, one for intermediate temperature fuel cells (ITFCs) working at 150-400 °C, e.g. NH₄PO₃¹⁴⁻¹⁶, and the other one for proton-conducting SOFCs working at 500-600 °C, e.g. BaCeO₃ and BaZrO₃ based materials¹⁷⁻¹⁹. The proton-containing (upon exposure to H₂O) ceramics under study are perovskites BaZr_{0.8}Y_{0.2}O_{2.9} (BZY20) and BaCe_{0.7}Zr_{0.1}Y_{0.1}Yb_{0.1}O_{3-δ} (BCZYYb). The steam concentration in the oxygen shuttle gas (H₂-H₂O), e.g. ~20% at 600 °C, is expected to create significantly high concentration of protons on the surface of perovskites through the H₂O-V_O^{••} (oxygen vacancy) interaction. The focus of the study is to study the battery performance using BZY20 and BCZYYb in ESM and compare them with the baseline ZrO₂. The underlying mechanisms of proton-mediated energy storage enhancement are also proposed.

The phase purity of the as-synthesized SO, Fe₂O₃-impregnated SO and reduced Fe₂O₃/SO are confirmed by XRD patterns shown in Fig S1 of the Supporting Information (SI). After being coated with Fe(NO₃)₃ and heat-treated at 600 °C, Fig. S1 shows that Fe₂O₃ is the secondary phase to the original SO phase. However, the intensity and shape of each peak of the original SO phase become weaker and broader, implying that the SO are coated by a thin Fe₂O₃ layer, which can also be seen in the SEM image of as-synthesized SO and Fe₂O₃-coated SO in Fig. S2. The surface

^a Department of Mechanical Engineering, University of South Carolina, Columbia, SC 29208 United State.

^b School of Chemical Engineering and Technology, Tianjin University, Tianjin 300350 P.R. China

† E-mail: HUANG46@cec.sc.edu

Electronic Supplementary Information (ESI) available: [Experimental details; XRD data of ESM materials; SEM images; Cell performance; and TPR results]. See DOI: 10.1039/x0xx00000x

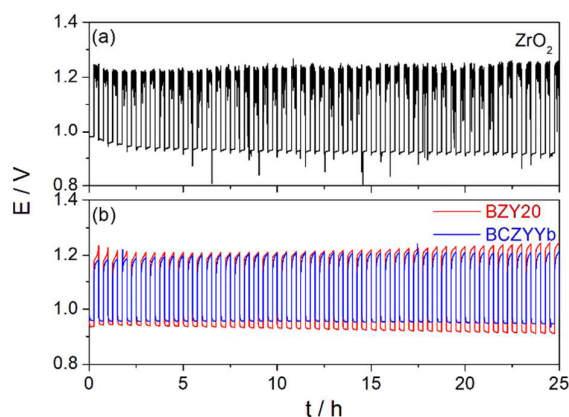
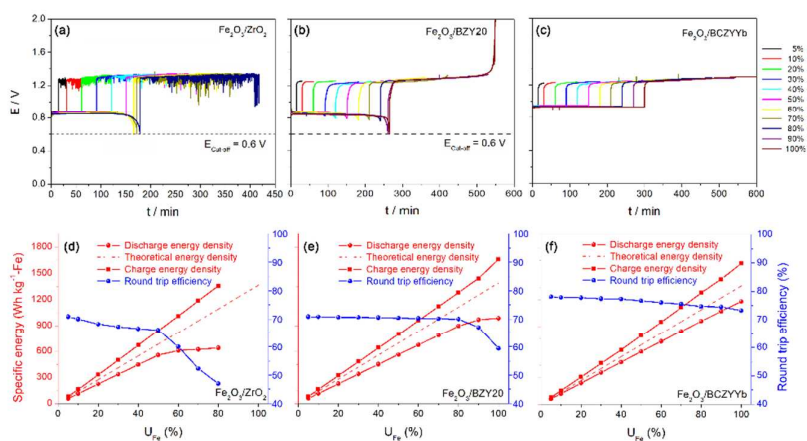


Fig. 1. Battery voltage profiles vs time. (a) Baseline ZrO₂ as SO and (b) proton-containing BZY20 and BCZYyb as SO.

of the original SO phase is coated with nanosized Fe₂O₃ particles, after reduction of which at 600 °C under a flowing H₂ atmosphere at 150 mL min⁻¹ for 2 h, Fig. S1 confirms that Fe₂O₃ has been reduced into Fe. Figure S3 shows that the reduction of Fe₂O₃ creates porosity in the Fe-bed (the volume shrinkage from Fe₂O₃ to Fe is 53.5%), which will benefit H₂/H₂O diffusion through the ESM bed.

To test the performance of SOMARB with different ESM materials, a 0.157 g of the Fe₂O₃-coated SO powders (with a total of Fe loading of 55 mg) were precisely weighted and placed in the fuel chamber³. Detailed description of cell assembly and testing can be found in our previous study³. Figure 1 compares the battery performance with different ESMs cycled at a constant current density of C/5 (1C = 1,272.7 mA g⁻¹ Fe, which is equivalent to 55.1 mA cm⁻² based on 1.27 cm² of active area of the cell) and a Fe utilization (U_{Fe}) of 5% (reference: at 1C and 100% U_{Fe}, it takes 1 h to oxidize all the Fe into FeO_x) at 550 °C. Figure 1a indicates that the battery performance with ZrO₂ as the SO phase is virtually non-rechargeable under the working condition. However, with



proton containing ceramics, BZY20

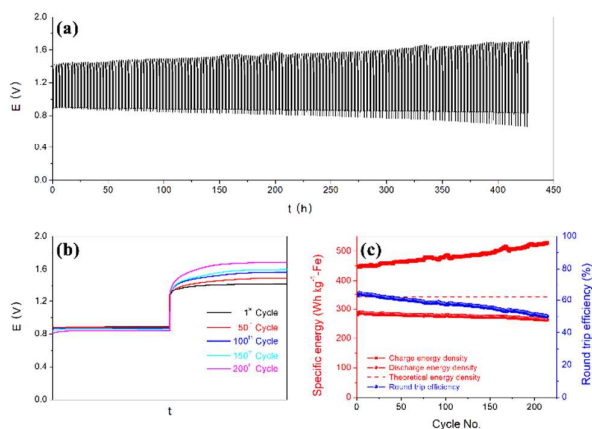


Fig. 2. Battery voltage profiles vs time with different SO-based ESMs, (a) ZrO₂; (b) BZY20; (c) BCZYyb; (e), (f), (g) corresponding specific energy and RTE vs U_{Fe} of (a), (b), and (c), respectively.

Fig. 3. Cycling performance of an IT-SOMARB with a BCZYyb proton-containing SO ESM, cycled at C/4 with U_{Fe} = 25%. (a) Battery voltage profiles vs time; (b) voltage profiles of selected cycles vs time; (c) discharge and charge specific energy and RTE vs cycle number

and BCZYyb, as the SO phase, the battery voltage is stable within 50 cycles tested under the same rate and U_{Fe}.

In addition, the three batteries were further tested under higher U_{Fe}, ranging from 5% to 100%, at C/5; the corresponding charging-discharging durations were 15 min and 5 h for 5% and 100% of U_{Fe}, respectively. The voltage profiles vs time for the three ESMs are shown in Fig. 2 (a)-(c), where the cut-off voltages were set to 0.6 and 2.0 V for the discharge and charge cycle, respectively. For the ZrO₂-SO ESM, Fig. 2 (d) shows that the battery can only be cycled at C/5 with a maximum U_{Fe} = 50%, but with considerable voltage fluctuations during the charging cycle. At U_{Fe} > 60%, the discharging voltage experiences a sharp decrease toward the end of the cycle. The round-trip efficiency (RTE) at 5% U_{Fe} reaches 71% and gradually drops to 66% and 47% at U_{Fe} = 50% and 100%, respectively.

For the BZY20-SO ESM, Fig. 2(e) shows that the highest U_{Fe} the battery can cycle at the same C/5 has been increased to 80%, below which the cycling voltage profiles remain flat. This clearly suggests that BZY20-SO ESM has a better reversibility than the ZrO₂-SO counterpart. The RTE at 5% U_{Fe} is 72%, and remains 70%, 67% and 59% at U_{Fe} = 80, 90 and 100%, respectively. For a higher proton-conductivity (or concentration) perovskite BCZYyb²⁰⁻²², Fig. 2 (f) shows that the battery's reversibility has been further improved; the battery can be cycled at a

utilization up to 100% without voltage collapse. The RTE reaches 78% at 5% U_{Fe}, and remains 73% for U_{Fe} = 100%. Clearly, BCZYyb-based Fe-ESM gives the best performance

among the three SO materials, implying the importance of proton concentration in the SO materials.

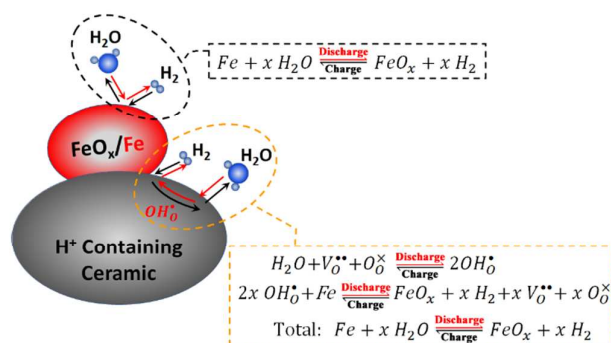
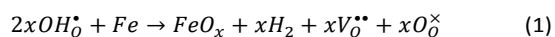


Fig. 4 A schematic illustrating the proton-mediated Fe redox reaction during a charge/discharge cycle.

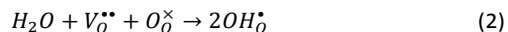
To demonstrate the long-term stability, the battery with BCZYb-SO ESM was further cycled at a higher current density, C/4 ($J=318.2 \text{ mA g}^{-1} \text{ Fe}$), with a higher $U_{Fe} = 25\%$, for over 200 cycles (total run time over 400 h). The results shown in Fig. 3a & b indicate that the average discharge voltage decreases slowly with time, roughly 8% after 214 cycles, but the average charge voltage increases faster with time (16% after 428 h). The discharge specific energy shown in Fig. 3c decreases from 282 to 264 Wh $\text{kg}^{-1}\text{-Fe}$, while the charge specific energy increases from 448 to 528 Wh $\text{kg}^{-1}\text{-Fe}$, resulting in an RTE decrease from 63% to 50% after over 200 cycles.

It is to be noted that the observed performance differences in Figs. 1-3 are dominantly related to the ESM since Fig. S4 in the SI explicitly shows that there is virtually no difference in RSOFC performance for the three batteries tested.

To understand the beneficial effect of proton-containing SO on the reversibility of the battery, we hypothesize in Fig. 4 a parallel pathway that mediates the oxidation of Fe and reduction of FeO_x through active proton-species in the proton-containing SO during a discharge cycle:

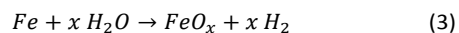


where the OH_O^* represents the active proton-species produced by the interaction between H_2O and oxygen vacancies V_O^* via ²³⁻²⁵:

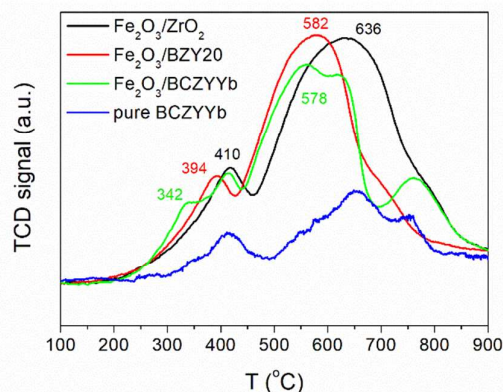


The hypothesis is that the produced, fast moving, active OH_O^* is transported through BCZYb (or BZY20) bulk to its interface with Fe, where it is then reduced by Fe to H_2 . The overall reaction is the same as described in reaction (3), which implies the proton-containing ceramic provides additional pathway to produce H_2 (during a discharge cycle). A reverse process is expected for the charge cycle.

In parallel, the conventional reaction of Fe with H_2O to form FeO_x (Fe_3O_4 at 550 °C) and release H_2 can take place at the surface of the Fe particles during the discharge cycle.



The simultaneous oxygen and proton pathways for Fe-redox reaction are the fundamental reasons for the enhanced



kinetics and reversibility of the battery.

Fig. 5 TPR profiles of different Fe_2O_3 -SO materials with a heating rate of 10 °C min^{-1} under 5% H_2 - N_2 carrying gas.

To confirm proton catalysing mechanism, temperature programmed reduction (TPR) was carried out on the Fe_2O_3 coated SO materials; the results are shown in Fig. 5. The first minor peak is related to the reduction of Fe_2O_3 to Fe_3O_4 ³, whereas the second primary peak is associated with the reduction of Fe_3O_4 to Fe. A comparison of the peak temperatures for all the three ESM materials suggest that $Fe_2O_3/BCZYb$ has the fastest kinetics toward H_2 -reduction as it exhibits the lowest peak temperature. From TPR profiles collected at different ramping rates, Fig. S5a-c shows linear plots of $\ln(\varphi/T_{max}^2)$ vs $1/T_{max}$, from whose slope the activation energy E_a of the reduction process is calculated out ²⁶ and shown in Fig. S5d. Again, $Fe_2O_3/BCZYb$ and $Fe_2O_3/BZY20$ exhibit lower E_a than Fe_2O_3/ZrO_2 , further suggesting that protons in BCZYb and BZY20 facilitate the Fe_2O_3 -reduction kinetics. This is also indirectly supported by the three similar peaks on the TPR profile of a pure BCZYb, which are related to the lattice oxygen release, forming oxygen vacancies²⁷; the latter will further promote the formation of OH_O^* in the presence of water vapour.

Conclusions

In summary, two proton-containing ceramics, namely BZY20 and BCZYb, have been successfully demonstrated as better SOs than ZrO_2 -based materials in ESM for SOMARB. The presence of proton in BZY20 and BCZYb significantly enhances the kinetics of redox reactions in ESM, thus the reversibility of SOMARB. The results show that BCZYb with the highest proton conductivity can achieve an RTE of 73% (at C/5) even at 100% Fe-utilization. The long-term cycle stability testing further shows that the battery with BCZYb as SO can cycle at C/4 and $U_{Fe}=25\%$ for more than 200 cycles, achieving a discharge specific energy of 282 - 264 Wh $\text{kg}^{-1}\text{-Fe}$ and an RTE of 50-63%.

Acknowledgements

The work is funded by the Advanced Research Projects Agency-Energy (ARPA-E), U.S. Department of Energy, under Award number DE-AR0000492.

Conflicts of interest

There are no conflicts to declare.

Notes and references

- N. Xu, X. Li, X. Zhao, J. B. Goodenough and K. Huang, *Energy & Environmental Science*, 2011, **4**, 4942-4946.
- X. Zhao, N. Xu, X. Li, Y. Gong and K. Huang, *RSC Advances*, 2012, **2**, 10163-10166.
- C. Zhang and K. Huang, *ACS Energy Letters*, 2016, **1**, 1206-1211.
- X. Zhao, X. Li, Y. Gong and K. Huang, *Chemical Communications*, 2014, **50**, 623-625.
- X. Zhao, Y. Gong, X. Li, N. Xu and K. Huang, *Journal of The Electrochemical Society*, 2013, **160**, A1241-A1247.
- X. Jin, X. Zhao, C. Zhang, R. E. White and K. Huang, *Electrochimica Acta*, 2015, **178**, 190-198.
- X. Zhao, N. Xu, X. Li, Y. Gong and K. Huang, *ECS Transactions*, 2013, **50**, 115-123.
- X. Zhao, X. Li, Y. Gong, N. Xu, K. Romito and K. Huang, *Chemical Communications*, 2013, **49**, 5357-5359.
- C. Zhang, C. Ji, W. Wang, D. Schmidt, X. Jin, J. P. Lemmon and K. Huang, *Energy & Environmental Science*, 2016, **9**, 3746-3753.
- R. D. McKerracher, C. Ponce de Leon, R. G. A. Wills, A. A. Shah and F. C. Walsh, *ChemPlusChem*, 2015, **80**, 323-335.
- X. Jin, X. Zhao, R. E. White and K. Huang, *ECS Transactions*, 2015, **68**, 251-268.
- X. Zhao, X. Li, Y. Gong, N. Xu and K. Huang, *RSC Advances*, 2014, **4**, 22621-22624.
- X. Jin, X. Zhao and K. Huang, *Journal of Power Sources*, 2015, **280**, 195-204.
- C. Sun, L. Chen, S. Shi, B. Reeb, C. A. López, J. A. Alonso and U. Stimming, *Inorganic chemistry*, 2018, **57**, 676-680.
- C. Sun, C. A. López and J. A. Alonso, *Journal of Materials Chemistry A*, 2017, **5**, 7839-7844.
- C. Sun and U. Stimming, *Electrochimica Acta*, 2008, **53**, 6417-6422.
- K. Kreuer, *Annual Review of Materials Research*, 2003, **33**, 333-359.
- N. Mahato, A. Banerjee, A. Gupta, S. Omar and K. Balani, *Progress in Materials Science*, 2015, **72**, 141-337.
- S. Haile, G. Staneff and K. Ryu, *Journal of Materials Science*, 2001, **36**, 1149-1160.
- T. Ishiyama, H. Kishimoto, K. Develos-Bagarinao, K. Yamaji, T. Yamaguchi and Y. Fujishiro, *Inorg Chem*, 2017, **56**, 11876-11882.
- L. Yang, S. Wang, K. Blinn, M. Liu, Z. Liu, Z. Cheng and M. Liu, *Science*, 2009, **326**, 126-129.
- S. Fang, K. Brinkman and F. Chen, *ACS applied materials & interfaces*, 2014, **6**, 725-730.
- E. Fabbri, D. Pergolesi and E. Traversa, *Chemical Society reviews*, 2010, **39**, 4355-4369.
- K. D. Kreuer, *Annual Review of Materials Research*, 2003, **33**, 333-359.
- Y. Yamazaki, P. Babilo and S. M. Haile, *Chemistry of Materials*, 2008, **20**, 6352-6357.
- H.-Y. Lin, Y.-W. Chen and C. Li, *Thermochimica Acta*, 2003, **400**, 61-67.
- S. Ricote, A. Manerbin, N. P. Sullivan and W. G. Coors, *Journal of Materials Science*, 2014, **49**, 4332-4340.